The Journal of Chemical Physics

RESEARCH ARTICLE | JANUARY 02 2026

Pore-collapse in amorphous solid water: A dynamics study

Special Collection: Carlos Vega Festschrift

Tobias Eklund ; Christina M. Tonauer ; Keishiro Yamashita ; Johannes Giebelmann ; Lilli-Ruth Fidler ; Aigerim Karina ; Hailong Li ; Louisa Kraft ; Fiona Berner; Niels C. Gießelmann ; Robert Bauer; Alexander Gierke ; Claudia Goy ; Marjorie Ladd-Parada ; Fivos Perakis ; Fabian Westermeier ; Felix Lehmkühler ; Thomas Loerting ; Katrin Amann-Winkel

J. Chem. Phys. 164, 014501 (2026)
https://doi.org/10.1063/5.0305153

AIP Publishing

The Journal of Chemical Physics ARTICLE pubs.aip.org/aip/jcp

Pore-collapse in amorphous solid water: A dynamics study

Cite as: J. Chem. Phys. 164, 014501 (2026); doi: 10.1063/5.0305153
Submitted: 3 October 2025 • Accepted: 13 December 2025 •
Published Online: 2 January 2026

Tobias Eklund,[1,2,3] Christina M. Tonauer,[4,5] Keishiro Yamashita,[5] Johannes Giebelmann,[5] Lilli-Ruth Fidler,[5] Aigerim Karina,[6] Hailong Li,[2] Louisa Kraft,[1,2] Fiona Berner,[1,2] Niels C. Gießelmann,[1,2,4] Robert Bauer,[4] Alexander Gierke,[3,4] Claudia Goy,[4] Marjorie Ladd-Parada,[6,7] Fivos Perakis,[6] Fabian Westermeier,[4] Felix Lehmkühler,[4] Thomas Loerting,[5,a)] and Katrin Amann-Winkel[1,2,a)]

AFFILIATIONS

[1] Institute of Physics, Johannes Gutenberg University Mainz, Staudingerweg 7, 55128 Mainz, Germany
[2] Max Planck Institute for Polymer Research, Ackermannweg 10, 55128 Mainz, Germany
[3] European XFEL, Holzkoppel 4 22869, Schenefeld, Germany
[4] Deutsches Elektronen-Synchrotron DESY, Notkestraße 85, 22607 Hamburg, Germany
[5] Institute of Physical Chemistry, University of Innsbruck, 6020 Innsbruck, Austria
[6] Department of Physics, Albanova University Center, Stockholm University, SE-10691 Stockholm, Sweden
[7] Department of Chemistry, KTH Royal Institute of Technology, SE-100 44 Stockholm, Sweden

Note: This paper is part of the Special Topic, Carlos Vega Festschrift.
[a)] **Authors to whom correspondence should be addressed:** thomas.loerting@uibk.ac.at and amannk@mpip-mainz.mpg.de

ABSTRACT

Vapor-deposited amorphous ice, so-called amorphous solid water, exhibits complex structural and morphological transformations upon heating. A network of micropores, present at the deposition temperature (80 K), collapses at 100–145 K, and a glass transition takes place simultaneously above 120 K. Here, we separate the two processes by allowing the micropores to collapse upon heating, which is monitored by small-angle x-ray scattering experiments. The combined micropore collapse and glass transition dynamics are studied using x-ray photon correlation spectroscopy. After cooling back down and heating a second time, we see remaining pores collapsing only near T_g. Our analysis reveals both diffusive and ballistic processes attributed to pore collapse dynamics. Fast processes (~100 Å^2/s) occur only when both micropore collapse and glass transition are simultaneously at play. In other words, both processes impact on each other and lead to a speed-up. The glass transition dynamics mainly features a slow diffusive process with a diffusion coefficient of around 1 Å^2/s and lower. This value is in nice agreement with other work on thin and on bulk samples.

INTRODUCTION

Amorphous solid water (ASW) is the most abundant form of water in the universe.[1] It is a non-crystalline form of ice that exists as the cover on interstellar dust grains and icy bodies such as comets or planetary moons.[2,3] ASW was directly detected in dark interstellar clouds based on its infrared absorption.[4] On Earth, temperatures are typically too high for ASW to exist because it crystallizes above 130–150 K,[5–11] producing nano-crystalline[12] or stacking-disordered ice, I_{sd}.[13] The only exceptions are the Earth's upper mesosphere in winter, where temperatures sometimes drop below 120 K. Even though this part of the atmosphere is very dry (mixing ratio of water of 1 ppm at a total pressure of 0.01 mbar), water vapor condenses as ASW there. This results in very thin ASW clouds that are hard to observe and known as noctilucent clouds.[14] The other exception is laboratories, where ASW is produced by the deposition of water vapor in high or ultrahigh vacuum on cold substrates typically kept in the range 10–130 K. The first to realize ASW as a deposit were

Burton and Oliver in the 1930s.[15] An additional important mechanism for ASW formation is the reaction of atoms with diatomic moieties, e.g., H with OH,[16] or H_2 with O.[17]

Unlike crystalline ice, ASW lacks long-range order just like other amorphous ices made from liquid droplets[18] or by pressurizing ice.[19] The vitrification of H_2O droplets requires hyperquenching and leads to a glassy state with a low density of 0.94 g/cm^3.[20,21] Pathways involving pressure-induced amorphization lead to amorphous ices of 25% to 40% higher density.[22] Our current study focuses on ASW made by the technique pioneered by Mayer and Pletzer,[18] which features much higher deposition rates than other vapor-deposition techniques and thereby allows for the production of gram quantities of ASW. ASW has been the subject of intense experimental[10,18,23–26] and theoretical interest.[27] The low-temperature deposition of water vapor onto cold substrates (~10–80 K) yields porous ASW structures that are often called p-ASW.[28–33] At higher temperatures, the ASW structure can be annealed into more compact, less porous forms often denoted as c-ASW.[9,32–34] These transformations not only are structurally informative but also impact the material's reactivity, volatility, and capacity to host small molecules.[18,35–37] ASW is particularly significant in the astrophysical context. It is the dominant form of water in cold interstellar and circumstellar environments, where it coats dust grains and acts as a reactive matrix for complex molecule formation under UV and cosmic-ray irradiation.[38,39]

Specific deposition conditions, especially background pressure and type of flow, and substrate interactions determine the resultant ASW porosity, co-deposition of background gas, and its evolution during heating.[18,29,34,40] Typically, lower deposition temperatures produce more porous samples, featuring specific surface areas of up to 1000 m^2/g.[41] Using the BET nitrogen adsorption method, the pores were characterized as micropores, with typical diameters of 2 nm.[35–37] Upon heating, the pores experience a collapse that was studied using a range of methods, including positron annihilation spectroscopy[42] and small-angle neutron scattering.[9,34] This collapse takes place below 150 K, before crystallization of the amorphous matrix. Even after the collapse of the micropores, some porosity remains, as indicated by near-infrared markers for porosity.[43] This porosity is even evident after crystallization of the ice. Guinier–Porod analysis of small-angle neutron data suggests that the pores are initially cylindrical (3D) and then collapse along one axis, leaving behind lamellae (2D) at crystallization.[9] This type of collapse is sketched in Fig. 1(a).

The glass transition of ASW has been observed below 150 K, in the same temperature range as the pore collapse. In terms of calorimetry, a heat capacity rise at 136 K was observed at a heating rate of 30 K/min and attributed to the glass transition temperature T_g.[44,45] Using dielectric relaxation spectroscopy, the "emergence of the expected α-relaxation peak of a liquid at $T > T_g$, whose completion is terminated by the onset of crystallization to cubic ice" was inferred.[46] These findings were later confirmed by more comprehensive measurements in a large frequency range, where ASW above its T_g was found to be of very low kinetic fragility[47] and to show a huge isotope effect on dynamics, suggesting an important role of nuclear quantum effects.[48] Using infrared spectroscopy, the glass transition could also be observed in ASW nanoscale films,[24,49] and the diffusion coefficient near T_g was estimated to be 6×10^{-21} m^2/s.[26] Depending on the specific rates employed in the experiment, the glass transition ranges from an onset of about 120 K (for heating rates of 10 K/h)[50,51] to over 174 K (for heating rates of 3×10^4 K/s).[52,53] A key aspect for understanding the dynamic processes within ASW upon heating is the fact that there are two superimposed types of dynamics: (i) dynamics related to the micropore collapse process and (ii) dynamics inherent to the water molecules in the bulk of ASW. That is to say, the dynamics of pore collapse and the molecular dynamics at the glass transition are intertwined and need to be disentangled. This has not been attempted in previous work and is, therefore, the key aim in the present study.

To separate the directed pore collapse and the translational motion of water molecules during the glass transition, we heat the porous ASW (p-ASW) in the first step to turn it into a more compact ASW (c-ASW). p-ASW features both types of dynamics, and we observe both in our first heating scan. In the second step, we cool c-ASW back down, where now the collapsed network of lamellae is present. That is, in c-ASW, the dynamics related to the pore collapse is largely suppressed if not fully absent. In the second heating scan, we then investigate the dynamics in the bulk, with only minor contributions from effects related to the pores and surface boundaries. We here use x-ray photon correlation spectroscopy (XPCS) to study the nanoscale dynamics of both processes, pore collapse and bulk dynamics of water molecules in porous ASW and bulk dynamics of water molecules in compact ASW. The main goal of this study is to disentangle the different dynamic processes related to pore collapse and diffusion, both below and above the glass transition temperature.

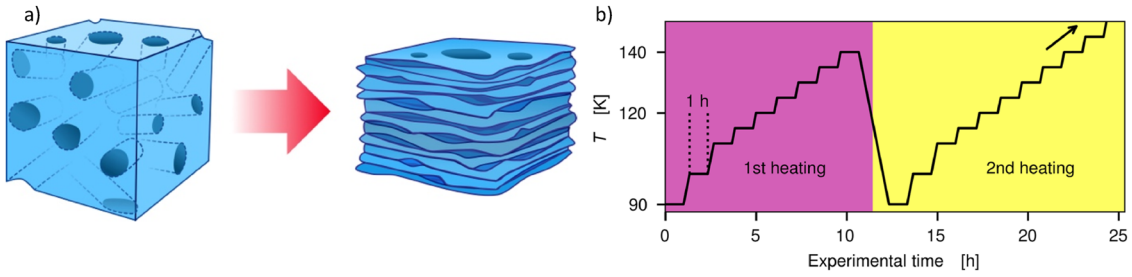

FIG. 1. (a) Cartoon of an ice cube with cylindrical pores inside. During heating, the pores collapse into a more compact, but heterogeneous and lamellar structure. (b) Experimental protocol. The temperature is raised in steps, allowing for measurements at constant temperature. The ASW pores collapse during the first heating.

METHODS

Sample preparation

In the present study, porous amorphous solid water (p-ASW) is prepared by direct, i.e., unbaffled vapor deposition in a high-vacuum glass apparatus developed by Mayer and Pletzer (see Fig. 2 of Ref. 18). H_2O vapor from a reservoir of liquid, ultrapure and degassed water, is introduced into the glass chamber via a 10 cm long copper nozzle (Ø = 1.3 cm). This nozzle is in line of sight of a liquid nitrogen-cooled copper plate at a distance of ~11 cm from the nozzle exit. At a deposition pressure of 5×10^{-1} mbar (minimum background pressure is 1.5×10^{-5} mbar), ASW is deposited for 1.5 h at ~80 K, yielding an ~ mm thick amorphous layer.[43] For sample recovery, an overpressure of dry gaseous argon is applied to vent the chamber, allowing for the removal of the cryo-plate and immediate immersion in liquid nitrogen, avoiding exposure to air. The deposit is scratched off the copper plate and recovered while under liquid nitrogen.

The deposition method results in a porosity of ~60%.[43] Direct, collimated molecular beam deposition perpendicular to the substrate surface is known to produce dense and compact c-ASW under UHV conditions.[10,54] Our samples, however, were produced under different conditions: Under high-vacuum conditions, water enters the chamber as a vapor stream via a large deposition orifice. This stream of water vapor cools down upon supersonic expansion, forming water clusters of various sizes.[18] When these clusters deposit on the surface, they form highly porous ASW.

Afterward, the scratched deposit is powdered in a liquid nitrogen bath and cold-loaded at LN_2 temperature to our sample holder. The sample holder is either (i) 2 μm thick diamond windows or (ii) a copper grid, into which the sample is pressed (free-standing in vacuum without confining diamond windows). At the beamline, the samples were mounted on a cold-finger cryostat (JANIS VPF-100). These methods were established in previous studies using the same cryostat environment.[25,55,56] The temperature was calibrated using our established protocol, described in detail in the supplementary material of Ref. 55. The given temperatures have an estimated error of ±2 K.

As described above, we expect the pores that have formed during the sample preparation to collapse during the first heating. This is, porous (p-)ASW transforms to a more compact (c-) ASW during heating, as sketched in Fig. 1(a). The protocol during the x-ray experiment follows the scheme depicted in Fig. 1(b). We heat the sample in steps of 5–20 K, with each temperature held for around an hour, collecting three datasets of 1000 s, naturally reaching different states of equilibration at a certain annealing time. The samples were heated from around 90 K to around 140 K [first heating, red area in Fig. 1(b)] and subsequently cooled down and remeasured in a second cycle using a similar protocol [second heating, yellow area in Fig. 1(b)].

Static and dynamic x-ray scattering (SAXS, XPCS, WAXS)

To study nanoscale dynamics during heating and annealing, we used x-ray photon correlation spectroscopy (XPCS).[57–60] In two beamtimes at beamline P10 of PETRA III (DESY, Hamburg), we collected data both in small-angle geometry (SAXS) and in ultra-small-angle geometry (USAXS), at sample–detector (Dectris EIGER X 4M) distances of 5 and 21 m, respectively. The scattering angle θ is calibrated using the known detector distance and converted to wave vector transfer, given by $(q = 4\pi \sin(\theta/2)/\lambda$ with x-ray wavelength λ). The SAXS measurement covers the q-range 3.1×10^{-3}–1.4×10^{-1} Å^{-1}. This range allows us to reveal the morphology of the sample, in terms of surface area, pore size, and shape at a length scale of 45 Å. For the SAXS measurements, the sample is held between diamond windows, as described above. The USAXS measurement covers a smaller q-range (1.7×10^{-3}–1.8×10^{-2} Å^{-1}, divided into 12 q-bins) and tracks changes at slightly larger length scales in real space. The advantage of using USAXS geometry is an increased scattered intensity, and therefore, improved statistics over the detector, while the larger x-ray spot size (unfocused beam of around $100 \times 100\ \mu m^2$) helps mitigate potential beam-induced damage. In USAXS mode, we use a free-standing sample suspended by a copper grid.

To obtain additional information on the water structure, a second detector was mounted close to the sample (15–30 cm) at a diffraction angle of ~30°. Hence, we are able to collect data simultaneously in both wide-angle scattering (WAXS) and SAXS/USAXS geometries. The WAXS measurement probes smaller length scales, giving the molecular structure of the sample, allowing us to identify the presence of an amorphous and/or crystalline structure.

From the SAXS data, the specific surface area, S, according to Porod's law is expressed as follows:

$$I(q) \sim Sq^{-4}. \tag{1}$$

A plot of $q^4 \cdot I$ vs q [the so-called Porod plot, Fig. 2(a)] reveals the asymptotic behavior at high q. We use an average over the highest available q-range (in SAXS) as a lower bound on the specific surface area,

$$S = \left\langle q^4 \cdot I(q) \right\rangle_{q \in [0.12\ \text{Å}^{-1}, 0.14\ \text{Å}^{-1}]}. \tag{2}$$

The uncertainty (and the error bars presented in the Results and discussion section) is taken to be the sample standard deviation within the same values of q. Measurements are taken at varying positions within the sample. To account for the inhomogeneous sample thickness, the scattering intensity was first normalized by the Porod invariant Q,

$$\begin{cases} I(q) = \dfrac{I'(q)}{Q}, \\ Q = \displaystyle\int q^2 I'(q)\ \mathrm{d}q. \end{cases} \tag{3}$$

Here, $I'(q)$ is the non-normalized input data. For this normalization, we used all the available intensity data from the SAXS and WAXS detectors combined.

The XPCS experiments rely on the coherence properties of modern synchrotron radiation sources, such as PETRA III. If the sample is static during the exposure of a coherent x-ray beam, the obtained scattering pattern shows a grainy structure, the so-called speckles. Sample dynamics are then given by the fluctuation of the speckle patterns' intensity, tracked by the correlation function of a series of images,

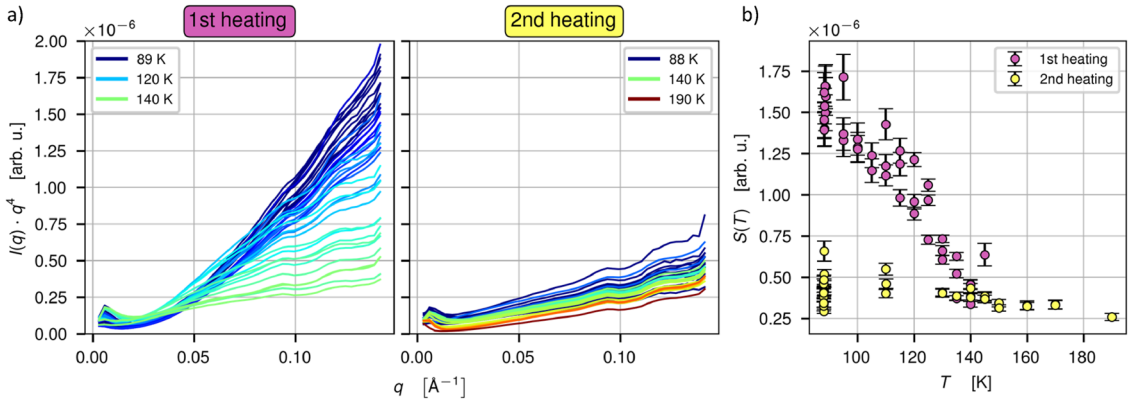

FIG. 2. X-ray scattering intensity showing the change in morphology during heating. (a) The scattering intensity is scaled by q^4 to show the specific surface area as the asymptotic tendency according to Porod's law. The temperature is increased in increments of 5 K during the first heating. During the second heating, the temperatures are 88, 110, and 130 K, followed by 5 K increments up to 190 K. (b) Specific surface area S calculated as the average of $I \cdot q^4$ over the range 0.12–0.14 Å^{-1}. This dataset was collected in SAXS geometry.

$$g_2(q,\tau) = \frac{\langle I(q_{\text{pix}},t)I(q_{\text{pix}},t+\tau)\rangle_{t,\text{pix}}}{\langle I(q,t)\rangle_{t,\text{pix}}}. \tag{4}$$

The averaging is performed over times t and detector pixels that belong to the same q-bin (averaging over time before pixels). The g_2 function is related to the intermediate scattering function (ISF) $F(q,\tau)$, which describes the temporal evolution of the sample, via the Siegert relation,

$$g_2(q,\tau) = 1 + \beta(q)|F(q,\tau)|^2, \tag{5}$$

where the speckle contrast for each q-bin, $\beta(q)$, depends on the coherence properties of the radiation.

For randomly walking particles, the intermediate scattering function is exponentially decaying with q^2 and the mean square displacement,[61]

$$F(q,\tau) = \mathrm{e}^{-\mathrm{MSD}(\tau)\ q^2/6}. \tag{6}$$

The most common observations in soft matter are Brownian diffusion (MSD = $6D\tau$) and ballistic motion [MSD = $6(v\tau)^2$]. The diffusive character is typical for particles in a liquid, while ballistic motion signifies stress-dominated dynamics that are present in many glasses. Note that the here obtained relaxation times τ at small q-values are not directly comparable to relaxation times from, for example, dielectric spectroscopy, because at small q, we are not probing the self-diffusion of single molecules directly. For this purpose, experiments at higher q-values or at the structure factor position of q = 1.7 Å^{-1} would be necessary. Here, instead, we probe the collective diffusion on nanometer length scales, which is sensitive to translational motion due to the sensitivity of the x rays to the electron density rather than the rotation of molecules.

For many applications, the ISF (and thus g_2) is described by a stretched (or compressed) exponential,

$$F(q,\tau) = \mathrm{e}^{-2(\Gamma(q)\ \tau)^\gamma}. \tag{7}$$

The relaxation rate $\Gamma(q)$ is then fit to a power-law q-dependence, with the relation $\Gamma = D_p q^p$. Here, $p = 2$ corresponds to the diffusive case discussed above, while $p = 1$ gives ballistic motion. In some cases, multiple distinct relaxations appear. Those are then modeled by weighted sums such as $F(q,\tau) = aF_1(q,\tau) + (1-a)F_2(q,\tau)$ for the case of two contributions.[55,56,62] This approach fails when the dynamic heterogeneities (i.e., different relaxation times from different domains in the sample) are not well captured by the stretching/compression parameter γ, and when the number of distinct relaxations to assume present (F_1, F_2, etc.) is unclear.

For an unknown population of scatterers, one may instead hypothesize an integral over a population density, such as[63,64]

$$F(q,\tau) = \int \Phi(D)\mathrm{e}^{-Dq^2\tau}\mathrm{d}D, \tag{8}$$

for particles undergoing Brownian diffusion. This gives a global model to be optimized against q and τ simultaneously for all q-bins. In the present case, we expect to find ballistic modes, diffusive modes, or a simultaneous mix of both. This results in the integral equation,

$$g_2(q,\tau) = 1 + \beta(q)\left(\underbrace{\int \Phi(D)\mathrm{e}^{-Dq^2\tau}\mathrm{d}D}_{\text{Diffusive component}} + \underbrace{\int \Psi(v)\mathrm{e}^{-(vq\tau)^2}\mathrm{d}v}_{\text{Ballistic component}}\right)^2, \tag{9}$$

which is to be solved to recover the density functions $\Phi(D)$ and $\Psi(v)$ for given input data g_2.

In practice, the solution to Eq. (9) is found by a best-fit procedure. The intermediate scattering function is discretized according to

$$F(q_i,\tau_j) = \sum_m \Phi_m \Delta D_m \mathrm{e}^{-D_m q_i^2 \tau_j} + \sum_m \Psi_m \Delta v_m \mathrm{e}^{-v_m q_i^2 \tau_j^2}, \tag{10}$$

and the coefficients Φ_m and Ψ_m are determined by least squares fitting to the recorded g_2 data. We allow a time-constant q-dependent baseline, which can absorb systematic errors caused by parasitic scattering. The full model is written out as

$$g_2(q_i,\tau_j) = 1 + b_i + \beta_i\left(\sum\nolimits_m \Phi_m \Delta D_m e^{-D_m q_i^2 \tau_j} + \sum_m \Psi_m \Delta \nu_m e^{-\nu_m q_i^2 \tau_j^2}\right)^2. \quad (11)$$

This is similar to the established CONTIN MULTIQ[63] method, but with the difference that we are modeling g_2 directly, rather than analyzing an experimental estimate of F. The squaring in Eq. (11) necessitates a non-linear fitting procedure. Further motivation, as well as mathematical and implementation details, are given in a recent publication by Eklund *et al.*[65] For simplicity, we drop the index notation below and refer to the discrete weights $\Phi_m \Delta D_m$ as $\Phi(D)\Delta D$ in our results.

For a finely resolved discretization [many small steps m in Eq. (10)], this type of model is too flexible, and least-squares optimization leads to overfitted, highly complex, solutions. To control this, a regularizing side condition is introduced.[66,67] The quantity

$$R = \frac{1}{D_0^5}\int\left(\frac{d^2\Phi}{dD^2}\right)^2 dD + \frac{1}{\nu_0^5}\int\left(\frac{d^2\Psi}{d\nu^2}\right)^2 d\nu \quad (12)$$

is large when the distributions Φ and Ψ exhibit many maxima, but small when the solution is smooth [normalizing by $D_0 = 1/\left(q_{\max}^2 \tau_{\max}\right)$ and $\nu_0 = 1/(q_{\max}\tau_{\max})$, using the largest q and τ in the dataset, keeps the regularizer terms dimensionless]. In general, an overfitted solution that fits close to experimental noise exhibits small summed squared residuals (i.e., χ^2), but a large value for R. So, by requiring that R takes on a not-too-large value, overfitting tendencies can be punished, while the model stays flexible with respect to the overall shape of F (beyond the stretched/compressed exponential paradigm) and the number of maxima when needed. The appropriate size of the regularizer R is determined by a hypothesis test. The regularized solution is rejected only when the increase in χ^2 induced by the regularizer is much larger than any expected statistical variation.[65,66] In this way, we choose the least complex solution [with complexity measured according to Eq. (12)] consistent with the data.

RESULTS AND DISCUSSION

Static scattering

Figure 2(a) shows the normalized x-ray scattering intensity scaled by q^4 for the two heating cycles. This shows how the specific surface area evolves, as discussed under the Methods section. In earlier neutron scattering experiments, these Porod plots reached a plateau at around 0.15 Å^{-1} (low temperature) down to 0.10 Å^{-1} (high temperature).[34] The expected plateaus are not clearly visible within the smaller q-range available here, but a reduction in surface area is, nevertheless, apparent as a change in slope and a decrease in the highest q-range. We take an average of $I \cdot q^4$ over the range 0.12–0.14 Å^{-1} as an estimate of the specific surface area S (this may be considered a lower bound due to the missing higher q values). Figure 2(b) summarizes the morphological changes by showing the estimate of S as a function of temperature for the first and second heating.

The temperature-dependent drop in $q^4 \cdot I$ at high q, during the first heating [Fig. 2(a)], indicates a pore collapse occurring from 90 K to around 140 K. The decrease seems to be rather linear, i.e., pore collapse goes on continuously over the ca. 10 h of the first heating. In total, the specific surface area decreases by roughly a factor of 5–6 [Fig. 2(b)]. During the second heating, much less of this decrease is observed, indicating that the ice is mostly compacted. With the surface area compacted by over a factor of 5, we call the sample c-ASW during the second heating. However, a decrease in surface area occurs at 90–140 K, even in the second cycle. Upon further heating above 140 K, the sample crystallizes.

The molecular structure, during the dynamics (USAXS) experiment, was monitored by a second detector in WAXS geometry. Figure 3 shows the characteristic broad diffraction maximum for ASW centered at around 1.7 Å^{-1}. The p-ASW has minor contamination of crystalline ice, visible through Bragg reflections. In c-ASW (second heating), there is slightly more crystalline ice than in p-ASW. That is to say, at 140 K, the crystal growth rate starts to be minuscule so that the ice fraction grows very slowly within an hour at this temperature. That finding prompted us to cool back down from this temperature. In the second heating cycle, this tiny fraction remains relatively stable up to 140 K, where further slow growth is noted.

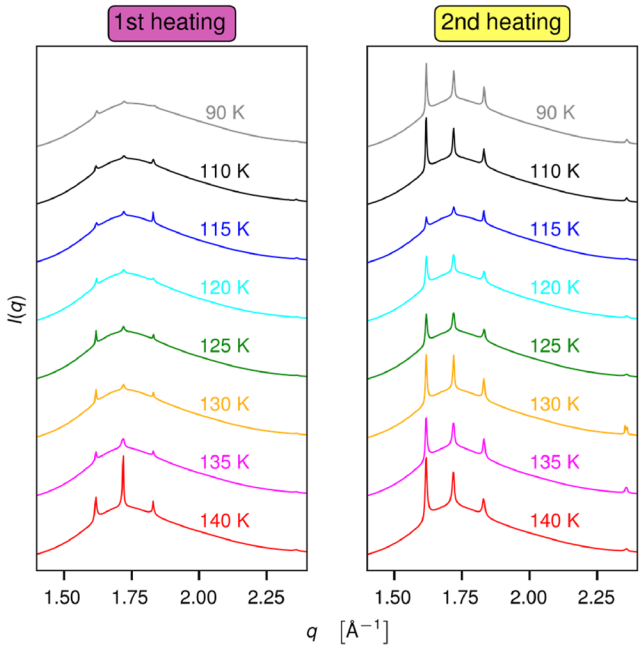

FIG. 3. WAXS scattering intensity during the XPCS measurements in USAXS geometry for both heating cycles. An offset has been introduced to facilitate comparison between results (y-axis is in arbitrary units). This figure shows a select measurement at each temperature. The same measurements for 115–140 K are used in the XPCS summaries of Figs. 4–6. The amorphous halo for ASW is centered at 1.7 Å^{-1}. Bragg reflections indicate crystalline contamination after the first heating cycle.

Dynamic scattering

Figure 4 shows selected intensity autocorrelation functions g_2 for different temperatures, following the protocol described in Fig. 1(b). At the lowest temperature (110 K), a rather fast decay is visible. Fitting the g_2 curve at 110 K (p-ASW) with a single stretched exponential decay [Eq. (7)] gives a relaxation time of around 200 s (at $q = 0.018$ Å^{-1}). At 120 K, more complex dynamics start to appear. These are not well described by a single exponential decay. The g_2 function, instead, gradually develops into a stepwise decay. During the first heating, this is most visible at 125 K (green curve in Fig. 4). After reaching 140 K, the sample was cooled back down to 80 K. The dynamics of the compacted ASW observed in the second heating are significantly slower than in p-ASW at 110–115 K (Fig. 4), with faster dynamics only reappearing at temperatures of 120 K (cyan) and 125 K (green).

The relatively fast, single relaxation at low temperatures (110–115 K) during the first heating presumably mainly pertains to the pore collapse happening at these temperatures. However, we associate the more complex dynamics at higher temperatures with both the pore collapse and dynamics in the H-bond network itself, hence the glass transition. The pore collapse somewhat saturates at the highest temperatures. The two-step decay during the second heating is again localized to temperatures close to the glass transition temperature for the heating rate employed here (the effective heating rate is ~6 K/h in both heating cycles). Most notably, the glass transition temperature of 124 K reported by Handa and Klug for slow heating Tian–Calvet calorimetry[50] and the one of 120 K reported by Amann-Winkel *et al.* for slow heating dielectric measurements[51]

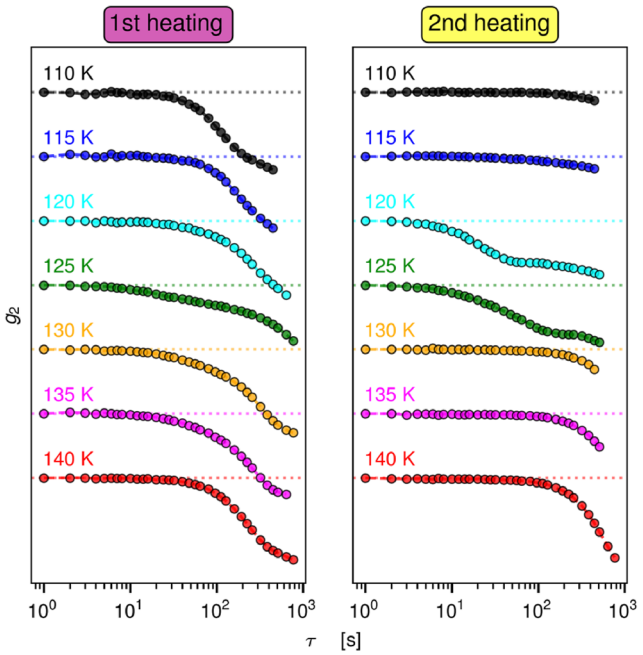

FIG. 4. Selection of g_2 curves recorded at different temperatures (q is 0.018 Å^{-1}) during the first and second heating. An offset has been introduced to facilitate comparison between results (y-axis is in arbitrary units).

are very close to the temperature at which we start to see a double decay in both heating runs. The crystalline ice, observed with WAXS, might also contribute to the overall dynamics, but it is expected to be a rather static component, with dynamics appearing outside our measuring window.[68] The data analysis of the complex g_2 functions has to be done carefully, as different microscopic processes are competing in the sample, namely, pore collapse, glass transition, and crystallization.

Given that we observe complex dynamics with at least two distinct relaxations with varying strength at temperatures above 115 K, we apply the global inverse transform technique described under the Methods section [Eqs. (8) and (9)]. As a working hypothesis, we expect the pore collapse to happen in a directed, ballistic manner, while the glass transition should exhibit some diffusive signal, assuming that the water molecules in a liquid undergo Brownian motion. Therefore, these heterogeneous dynamics may be decomposable into a ballistic and a diffusive component according to

$$F(q,\tau) = \underbrace{\int \Phi(D) e^{-Dq^2\tau} dD}_{\text{Diffusive component}} + \underbrace{\int \Psi(v) e^{-(vq\tau)^2} dv}_{\text{Ballistic component}}, \qquad (13)$$

as discussed for Eq. (9). This approach has not been applied to XPCS data on amorphous ice before.

Figure 5 shows results from applying this model to the p-ASW sample in the first heating cycle. We included data starting from 115 K, the temperature where a description with single exponential decays starts to fail (the 110 K measurements are, however, included in the summary of Fig. 7). The top and middle rows show discrete weights for diffusion rates D, with $\Phi(D)\Delta D$, and velocities v, with $\Psi(v)\Delta v$, for the diffusive (blue) and ballistic (red) components, respectively. These are further divided into fast and slow processes, for which the splitting points D_{split}, defined as the first stationary point $d\Phi/dD = 0$ after the first maximum, are shown as dashed vertical lines. After this classification, there are four distinct contributions: slow ballistic, fast ballistic, slow diffusive, and fast diffusive. The bottom row of Fig. 5 shows the intermediate scattering function, $F(q,\tau)$, plotted for five select q-values, with the full fast and slow processes (diffusive + ballistic) shown as black dashed lines (when the fast component is significant).

The results in Fig. 5 show that both diffusive and ballistic modes appear in the slow and fast processes. As shown in Fig. 4, the fast decays appear with increasing temperature starting from 120 K. Diffusive components also increase with temperature and are strongest at 125 K. At this temperature, the fast diffusive component at around 100 Å^2/s dominates. However, at 140 K, decays are mostly of the ballistic type again. There are a few cases of split peaks in the fast region of Ψ. This may be an artifact of the regularization procedure and should be interpreted with caution.[65] A description with just one fast peak (in a more central position) would likely produce a nearly identical fit. The division into fast and slow processes, however, is robust. An overall monomodal description would certainly fail to capture the two-step appearance of g_2.

Figure 6 shows the XPCS analysis result for the second heating cycle, after cooling to liquid nitrogen temperature. After re-heating to 115 K, the dynamics are very slow, to the point where there is

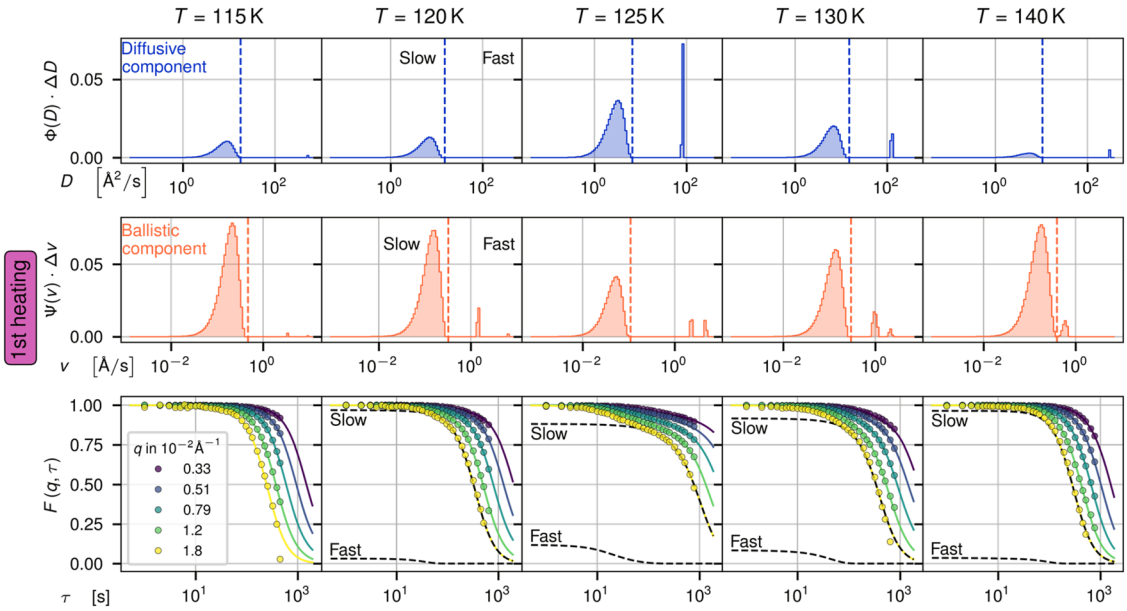

FIG. 5. First heating: heterogeneous dynamics of the intermediate scattering function F (bottom), decomposed into two components: a diffusive component (blue, top row) and a ballistic component (red, middle row). The results are split into fast and slow processes using the vertical dashed lines in the top and middle rows. The bottom row shows the data points transformed from g_2 to F according to the Siegert relation and the model result. The black dashed lines represent the lines of fit computed for the fast and slow processes separately, while the green-yellow solid lines represent the total lines of fit.

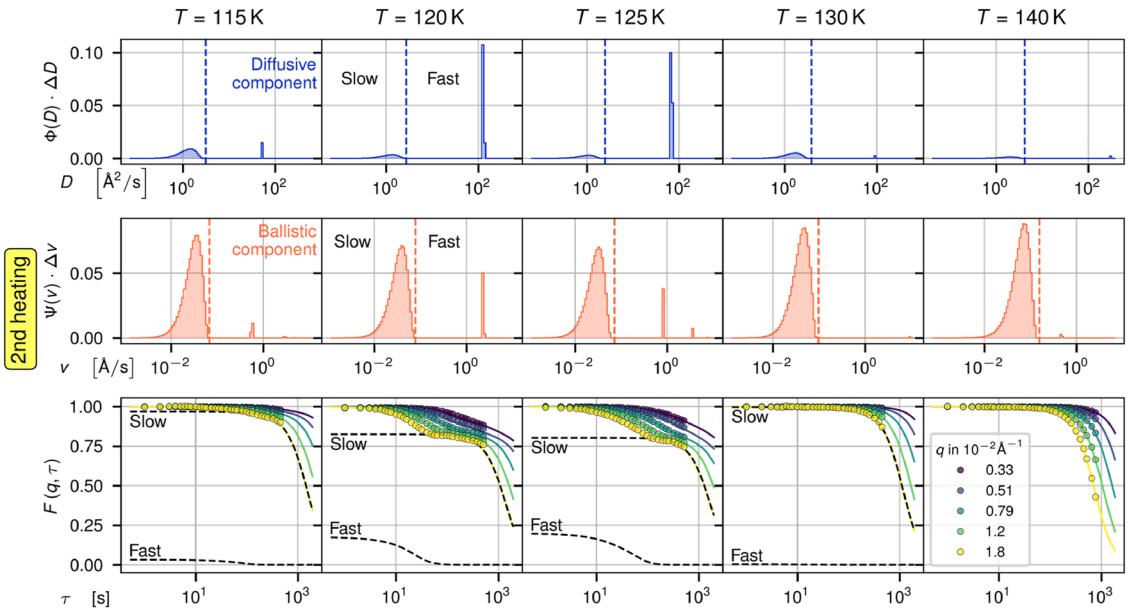

FIG. 6. Second heating: heterogeneous dynamics of the intermediate scattering function F (bottom), decomposed into two components: a diffusive component (blue, top row) and a ballistic component (red, middle row). The results are split into fast and slow processes using the vertical dashed lines in the top and middle rows. The bottom row shows the data points transformed from g_2 to F according to the Siegert relation and the model result. The black dashed lines represent the lines of fit computed for the fast and slow processes separately, while the green-yellow solid lines represent the total lines of fit.

barely any decay to analyze. The fitting procedure still favors a ballistic shape for the slow decay, but here we are sensitive to possible biases inherent in the modeling.[65] This means that the result concerning ballistic vs diffusive character for the slow process in the second heating should be considered highly uncertain at 115–130 K. The measurement at 140 K, however, is decaying significantly faster, and the ballistic-type result is derived from an adequate amount of data. We can still separate a fast process, with enough range in terms of delay times to analyze its ballistic vs diffusive character at every temperature. Here, during the second heating, the fast process reappears at 120 K and is better described by diffusive modes than ballistic modes at 120–125 K. At 130 K, the fast process vanishes.

For further analysis, we compute five more quantities from the distributions Φ and Ψ of Figs. 5 and 6. The total strength of the fast process,

$$W_F = \int_{D_{split}}^{\infty} \Phi \, dD + \int_{v_{split}}^{\infty} \Psi \, dv, \tag{14}$$

measures how much of F is accounted for by the first, fast step (values range from 0 to 1).

Given an existing fast process, the fast process diffusive proportion,

$$\frac{\int_{D_{split}}^{\infty} \Phi \, dD}{W_F}, \tag{15}$$

shows to what proportion it is explained by diffusive modes (not computed when $W_F < 0.01$). Finally, the median rates D and v are the medians computed for each split distribution separately (not computed for the fast process when $W_F < 0.01$). With these, we can summarize the XPCS results and attempt an interpretation of the data. The parameters for both heating runs are plotted in Fig. 7(a), where the first row shows the total strength W_F of the fast component and the second row shows the diffusive proportion. The fast component strength W_F increases with increasing temperature, particular at temperatures around 120 K. In the second heating, W_F vanishes at $T > 130$ K (Fig. 7, top row, right column). This goes along with a decrease in the diffusive proportion (middle row, right), and the slow ballistic component dominating at $T = 130$ K and $T = 140$ K (Fig. 6). The spread of the data at a constant temperature, from up to four XPCS measurements, can be explained by the equilibration effect mentioned under the Methods section (sample preparation). That is, measurements taken immediately after reaching a stable temperature exhibit faster relaxation rates than measurements taken after some aging at a constant temperature. With few exceptions, slower results are measured after a longer elapsed time. However, we note that the trends remain the same regardless of the spread of the data.

The median diffusion coefficients D of the fast and slow components are shown separately (Fig. 7, middle and bottom rows). For the fast component, D is rather constant (ignoring outliers) in both heating runs at values of around 100–300 Å^2/s (blue dashed line in third row), while the overall diffusive proportion and overall strength W_F only increases at $T > 120$ K (first heating) and $T > 115$ K (second heating). The fast process median (ballistic) velocity v (Fig. 7, row 4) is close to 1 Å/s. For the slow process, the median diffusion rate D (bottom row) is scattered around 3–10 Å^2/s in the first heating. It slows down to around 1 Å^2/s after cooling and

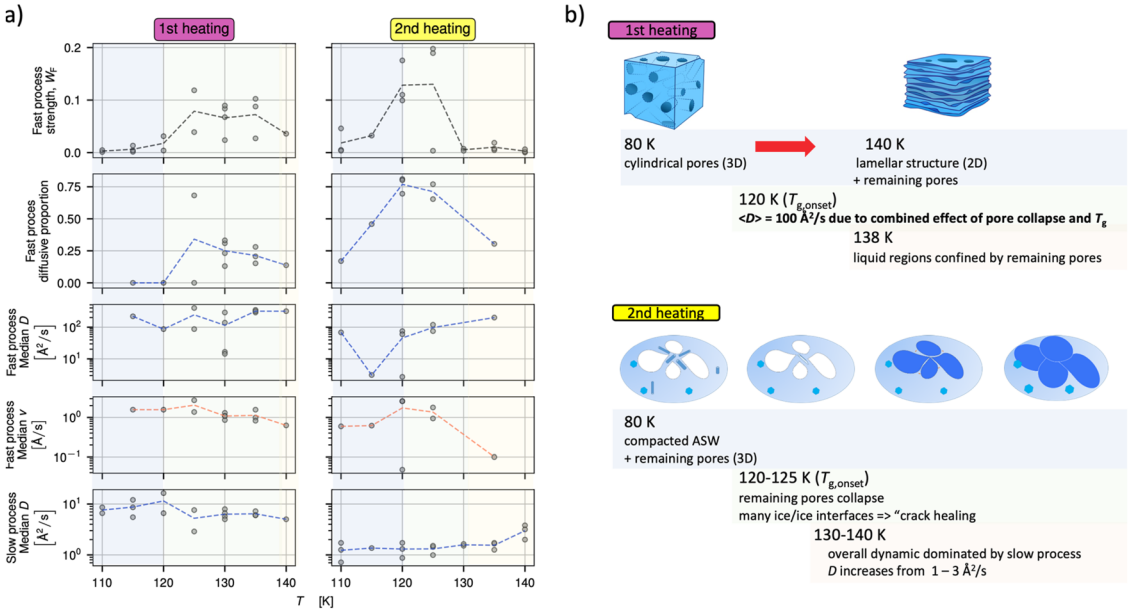

FIG. 7. Detailed analysis of XPCS data and physical interpretation. (a) Key characterizing quantities according to Eqs. (11) and (12) (first and second rows), and median rates of the slow and fast processes. The dashed lines are given by the average of the existing data points, as an indication of overall tendencies. Figure S1 of the supplementary material shows the fraction of diffusive vs ballistic modes for the slow process (similar to the second row here). (b) Summary and physical interpretation of the data.

subsequently increases with increasing temperature to 3 Å^2/s at 140 K. The related diffusive proportions are analyzed in Fig. S1. After the remaining pores collapsed in the second heating run, the diffusive proportion (Fig. S1) decreases significantly, because the process is too slow to cause a decay in $F(q,t)$ (see Fig. 6 at 130 K). Only the interplay of fast and slow processes allows us to extract values for the slow diffusive process with reasonable certainty.

In summary, during the first heating and the related pore collapse, we observe two simultaneous processes: one process in which molecules diffuse at a rate of around 3–10 Å^2/s, and a second process that is 100-times faster. Considering that the strength of the fast diffusive component increases at $T > 120$ K, and the SAXS results presented in Fig. 2(a), we propose that a combination of glass transition and pore collapse allows the water molecules to undergo motion with a median D of around 100–300 Å^2/s. The pore collapse has to be directional and, therefore, also has a ballistic component with a velocity $v \sim 1$ Å/s. During the first heating cycle, the porous structure contains a large area of ice–air interfaces. The pore collapse from three-dimensional cylindrical pores to two-dimensional lamellar structures is depicted in Fig. 7(b). At the highest temperatures, ultraviscous liquid regions will be confined by remaining pores as well as crystalline ice, which was observed in the WAXS data (Fig. 3). These liquid-like regions arrest during cooling to compact low-density amorphous ice [see the additional sketch in Fig. 7(b), white regions represent arrested amorphous ice patches, the light blue matrix is previously formed ASW with pores, and plates of crystalline ice]. While reheated, the remaining pores collapse, and new grain boundaries appear. Above the glass transition temperature of around 120 K, the fast diffusive component becomes maximal. The consecutive loss of the fast diffusive component at $T > 130$ K coincides with the completed micropore collapse [see the surface area S, Fig. 2(b), and sketches in Fig. 7(b)]. The collapsed pores lead to grain boundaries, and "crack healing" sets in when ultraviscous water forms. This shifts the detectable slow process almost out of our detectable time window for the designated q-range.

CONCLUSION

Vapor deposited amorphous ice is a highly porous material. Earlier small-angle neutron scattering studies[34] revealed a cylindrical porous structure and related its pore collapse (upon heating) to the appearance of a glass to liquid transition.[9] While the two processes of pore collapse and glass transition are clearly connected, our present study aims to disentangle the two processes. We prepared porous ASW samples through vapor deposition on a cold substrate. The SAXS data presented here show that the porous structure collapses upon heating to 140 K. The surface area decreases by a factor of 5–6 while heating, supporting earlier findings.[34] Subsequent cooling and re-heating reveal that the pore collapse is almost complete, as SAXS intensity and specific surface area drop only slightly during the second heating.

While SAXS measurements provide insights into the change in specific surface area, the timescale and related molecular dynamics of this thermally activated process are provided here from XPCS. During the first heating, at temperatures up to 115 K, the g_2 correlation curve decays with a single relaxation. The dynamics fully decorrelate over a measuring time of 1000 s (at $q = 0.018$ Å^{-1}). In this temperature range, the micropore collapse dominates. At 120 K, a double decay appears, which can be explained by the interplay of glass transition and pore collapse. At 140 K, the situation appears to become even more complex, as an increase in crystalline ice is observed from the WAXS pattern. The crystalline ice is expected to be a rather static component, which would appear outside our measuring window.[68] A second heating process followed after cooling the sample from 140 K back to 80 K. Clearly, the now compacted ASW coexists with remaining pores and small amounts of crystalline ice. The related g_2 curves at the lowest temperatures feature barely any decay until 120 K. Surprisingly, again a double exponential decay function occurs, which we relate to an interplay of the glass transition and remaining pores collapsing or at least a change in their morphology. The same scenario was observed during the first heating, while the micropore collapse was initiated at lower temperatures. At 130 K, the double decay disappears, and only a slow decay remains.

The process at intermediate temperatures cannot be described with a single exponential decay, and clearly several molecular and microscopic processes must be involved. To quantify these processes, we here use an analysis approach based on theoretical models of the intermediate scattering function $F(q,\tau)$. By performing a non-linear inverse transform of the intensity autocorrelation g_2, we derive best-fit weights for decays with diffusion rate D—assuming some Brownian motion—and velocity v—assuming one process to be ballistic.[65] From the experiment, we have access to a wide range of momentum transfer q. The analysis method accounts for this by optimizing the model against g_2 for all q-values simultaneously, in a surface fit manner. As a result, ballistic and diffusive decays both appear at a fast and a slow timescale. The values for the fast diffusive component are rather constant at $D = 100$–300 Å^2/s throughout all temperatures in both heating cycles, but increase in strength only at $T > T_g$ in both heating cycles. That is, the fast diffusive process resembles the pore collapse that is impacted by the glass transition inside the amorphous ice matrix, while it also contains a fast ballistic component. Both fast components vanish in the second heating cycle at $T > 130$ K. The slowed down dynamics in the second heating run at $T > 130$ K can be explained by two scenarios: (1) the pore collapse is finally completed, and the slow decay resembles the glass transition process in amorphous ice. (2) The crystalline ice fraction increases and starts interfering with the molecular motion. We expect scenario (1) to be more likely, as in previous studies,[55] the growth of crystalline ice was outside our experimental window and is expected to happen at even slower timescales at these temperatures.

While the pore collapse dominates during the first heating cycle, the slow diffusive component is rather fast (10 Å^2/s), comprising the effects of ice–air interfaces. Nevertheless, we relate the slow diffusive component to the glass transition dynamics within the amorphous ice matrix. During the second heating, median D increases from 1 to 3 Å^2/s. The slow ballistic component remains present throughout all temperatures and is related to overall stress relaxation in the sample, as observed also in other materials.[69] In the small-angle neutron scattering study by Hill *et al.*, they estimate a self-diffusion coefficient higher than 10^{-18} cm^2/s (= 0.01 Å^2/s) based on the time-dependence of the pore collapse at 120–136 K, consistent with our finding here.[9] Our values for D in the presented temperature range are further consistent with recent IR and TPD data from compact vapor deposited amorphous ice films (cASW), measuring intermixing of isotopic layer with D given as

6×10^{-21} m^2/s = 0.6 $Å^2/s$ at 136 K.[26,70] Other studies obtained the diffusivity from the crystalline growth rate[71] in such compact ASW films to be slightly lower but in good agreement.[26] The difference of less than a factor of 10 compared to the here presented data can easily be explained by the distinct morphology of the samples, i.e., thin film vs bulk samples and c-ASW vs a porous sample. We suggest the here reported diffusion rates to be rather an upper boundary for differently prepared ASW ice.

Measuring such slow processes by XPCS in USAXS geometry is difficult. Only the interplay of pore collapse and diffusion has pushed the detectable glass transition into our measurable time window, and the observed collective motion contains a diffusive part, which is sensitive to translational nanoscale dynamics.

In summary, we observe that the glass transition in ASW appears at $T > 120$ K, and the nanoscale motion appears in the order of $D = 1$ $Å^2/s$ and simultaneously impacts the 100 times faster dynamics of the micropore collapse.

SUPPLEMENTARY MATERIAL

The supplementary material contains additional information for Fig. 7 and shows the fraction of diffusive and ballistic modes for the slow process.

ACKNOWLEDGMENTS

We acknowledge Deutsches Elektronen-Synchrotron DESY (Hamburg, Germany), a member of the Helmholtz Association HGF, for the provision of experimental facilities. The measurements of this research were carried out at PETRA III, beamline P10. Beamtime was allocated for proposals under Grant Nos. I-20211355 and T-20220749. This research was supported in part by the Maxwell computational resources operated at DESY, Hamburg, Germany. T.E., C.M.T., R.B., and A.G. acknowledge funding by the Centre for Molecular Water Science (CMWS) within Early Science Projects. C.M.T. acknowledges funding by PIER - Partnership of University Hamburg and DESY within a PIER Seed Project (Grant No. PIF-2024-05), by the Austrian Academy of Sciences (ÖAW), and by the Austrian Science Fund (FWF) within the Disruptive Innovation-Early Career Seed Money Grant. N.C.G. acknowledges funding by the city of Hamburg in the research project "Control of the special properties of water in nanopores" (Grant No. LFF-FV68). K.Y. acknowledges funding by the Japan Society for the Promotion of Science (JSPS) within the Overseas Research Fellowships. We also thank Francesco Dallari for coding and support during beamtime and the scientific exchange and support within CMWS.

AUTHOR DECLARATIONS

Conflict of Interest

The authors have no conflicts to disclose.

Author Contributions

Tobias Eklund: Data curation (equal); Formal analysis (equal); Investigation (equal); Methodology (equal); Software (equal); Visualization (equal); Writing – original draft (equal); Writing – review & editing (equal). **Christina M. Tonauer**: Data curation (equal); Investigation (equal); Methodology (equal); Resources (equal). **Keishiro Yamashita**: Data curation (equal); Formal analysis (equal); Investigation (equal). **Johannes Giebelmann**: Data curation (equal); Investigation (equal); Writing – review & editing (equal). **Lilli-Ruth Fidler**: Data curation (equal); Investigation (supporting). **Aigerim Karina**: Conceptualization (equal); Data curation (equal); Investigation (equal). **Hailong Li**: Data curation (equal); Investigation (equal); Methodology (equal). **Louisa Kraft**: Data curation (equal); Investigation (equal). **Fiona Berner**: Data curation (equal); Investigation (equal). **Niels C. Gießelmann**: Data curation (equal); Investigation (equal). **Robert Bauer**: Data curation (equal); Investigation (equal); Writing – review & editing (supporting). **Alexander Gierke**: Data curation (equal); Investigation (equal). **Claudia Goy**: Data curation (equal); Investigation (equal). **Marjorie Ladd-Parada**: Data curation (equal); Investigation (equal); Writing – review & editing (equal). **Fivos Perakis**: Conceptualization (equal); Data curation (equal); Investigation (equal); Writing – review & editing (equal). **Fabian Westermeier**: Formal analysis (equal); Methodology (equal); Resources (equal); Software (equal); Writing – review & editing (supporting). **Felix Lehmkühler**: Formal analysis (equal); Funding acquisition (equal); Investigation (equal); Methodology (equal); Project administration (equal); Resources (equal); Supervision (equal). **Thomas Loerting**: Conceptualization (equal); Data curation (equal); Funding acquisition (equal); Investigation (equal); Methodology (equal); Project administration (equal); Resources (equal); Supervision (equal); Writing – original draft (equal); Writing – review & editing (equal). **Katrin Amann-Winkel**: Conceptualization (equal); Data curation (equal); Funding acquisition (equal); Investigation (equal); Methodology (equal); Project administration (equal); Resources (equal); Supervision (equal); Visualization (equal); Writing – original draft (equal); Writing – review & editing (equal).

DATA AVAILABILITY

Raw data were generated at beamline P10 of the PETRA III large scale facility in Hamburg, Germany. Derived data supporting the findings of this study are openly avilable in the Zenodo repository at https://doi.org/10.5281/zenodo.18010897.

REFERENCES

[1] A. C. A. Boogert, P. A. Gerakines, and D. C. B. Whittet, "Observations of the icy universe," Annu. Rev. Astron. Astrophys. **53**, 541–581 (2015).

[2] S. F. Newman, B. J. Buratti, R. H. Brown, R. Jaumann, J. Bauer, and T. Momary, "Photometric and spectral analysis of the distribution of crystalline and amorphous ices on Enceladus as seen by Cassini," Icarus **193**(2), 397–406 (2008).

[3] M. G. Fox-Powell and C. R. Cousins, "Partitioning of crystalline and amorphous phases during freezing of simulated Enceladus ocean fluids," J. Geophys. Res.: Planets **126**(1), e2020JE006628, https://doi.org/10.1029/2020je006628 (2021).

[4] A. Leger, J. Klein, S. de Cheveigne, C. Guinet, D. Defourneau, and M. Belin, "The 3.1 μm absorption in molecular clouds is probably due to amorphous H_2O ice," Astron. Astrophys. **79**, 256–259 (1979).

[5] R. H. Beaumont, H. Chihara, and J. A. Morrison, "Transitions between different forms of ice," J. Chem. Phys. **34**(4), 1456–1457 (1961).

[6]L. G. Dowell and A. P. Rinfret, "Low-temperature forms of ice as studied by X-ray diffraction," Nature **188**(4757), 1144–1148 (1960).
[7]J. A. Ghormley, "Enthalpy changes and heat-capacity changes in the transformations from high-surface-area amorphous ice to stable hexagonal ice," J. Chem. Phys. **48**(1), 503–508 (1968).
[8]J. P. Devlin, "Structure, spectra, and mobility of low-pressure ices: Ice I, amorphous solid water, and clathrate hydrates at $T < 150$ K," J. Geophys. Res.: Planets **106**(E12), 33333–33349, https://doi.org/10.1029/2000je001301 (2001).
[9]C. R. Hill, C. Mitterdorfer, T. G. A. Youngs, D. T. Bowron, H. J. Fraser, and T. Loerting, "Neutron scattering analysis of water's glass transition and micropore collapse in amorphous solid water," Phys. Rev. Lett. **116**(21), 215501 (2016).
[10]E. H. Mitchell, U. Raut, B. D. Teolis, and R. A. Baragiola, "Porosity effects on crystallization kinetics of amorphous solid water: Implications for cold icy objects in the outer solar system," Icarus **285**, 291–299 (2017).
[11]M. K. McClure, W. R. M. Rocha, K. M. Pontoppidan, N. Crouzet, L. E. U. Chu, E. Dartois, T. Lamberts, J. A. Noble, Y. J. Pendleton, G. Perotti, D. Qasim, M. G. Rachid, Z. L. Smith, F. Sun, T. L. Beck, A. C. A. Boogert, W. A. Brown, P. Caselli, S. B. Charnley, H. M. Cuppen, H. Dickinson, M. N. Drozdovskaya, E. Egami, J. Erkal, H. Fraser, R. T. Garrod, D. Harsono, S. Ioppolo, I. Jiménez-Serra, M. Jin, J. K. Jørgensen, L. E. Kristensen, D. C. Lis, M. R. S. McCoustra, B. A. McGuire, G. J. Melnick, K. I. Öberg, M. E. Palumbo, T. Shimonishi, J. A. Sturm, E. F. van Dishoeck, and H. Linnartz, "An ice age JWST inventory of dense molecular cloud ices," Nat. Astron. **7**(4), 431–443 (2023).
[12]M. Nachbar, D. Duft, and T. Leisner, "The vapor pressure over nano-crystalline ice," Atmos. Chem. Phys. **18**(5), 3419–3431 (2018).
[13]T. L. Malkin, B. J. Murray, C. G. Salzmann, V. Molinero, S. J. Pickering, and T. F. Whale, "Stacking disorder in ice I," Phys. Chem. Chem. Phys. **17**(1), 60–76 (2015).
[14]B. J. Murray and E. J. Jensen, "Homogeneous nucleation of amorphous solid water particles in the upper mesosphere," J. Atmos. Sol.-Terr. Phys. **72**(1), 51–61 (2010).
[15]E. F. Burton and W. F. Oliver, "The crystal structure of ice at low temperatures," Proc. R. Soc. Lond. A **153**(878), 166–172 (1935).
[16]F. Dulieu, L. Amiaud, E. Congiu, J.-H. Fillion, E. Matar, A. Momeni, V. Pirronello, and J. L. Lemaire, "Experimental evidence for water formation on interstellar dust grains by hydrogen and oxygen atoms," Astron. Astrophys. **512**, A30 (2010).
[17]M. Serra-Peralta, C. Domínguez-Dalmases, and A. Rimola, "Water formation on interstellar silicates: The role of Fe^{2+}/H_2 interactions in the $O + H_2 \rightarrow H_2O$ reaction," Phys. Chem. Chem. Phys. **24**(46), 28381–28393 (2022).
[18]E. Mayer and R. Pletzer, "Polymorphism in vapor deposited amorphous solid water," J. Chem. Phys. **80**(6), 2939–2952 (1984).
[19]O. Mishima, L. D. Calvert, and E. Whalley, "'Melting ice' I at 77 K and 10 kbar: A new method of making amorphous solids," Nature **310**(5976), 393–395 (1984).
[20]T. Loerting, M. Bauer, I. Kohl, K. Watschinger, K. Winkel, and E. Mayer, "Cryoflotation: Densities of amorphous and crystalline ices," J. Phys. Chem. B **115**(48), 14167–14175 (2011).
[21]D. T. Bowron, J. L. Finney, A. Hallbrucker, I. Kohl, T. Loerting, E. Mayer, and A. K. Soper, "The local and intermediate range structures of the five amorphous ices at 80 K and ambient pressure: A Faber–Ziman and Bhatia–Thornton analysis," J. Chem. Phys. **125**(19), 194502 (2006).
[22]K. Amann-Winkel, R. Böhmer, F. Fujara, C. Gainaru, B. Geil, and T. Loerting, "Colloquium: Water's controversial glass transitions," Rev. Mod. Phys. **88**(1), 011002 (2016).
[23]Y. Xu, N. G. Petrik, R. S. Smith, B. D. Kay, and G. A. Kimmel, "Homogeneous nucleation of ice in transiently-heated, supercooled liquid water films," J. Phys. Chem. Lett. **8**(23), 5736–5743 (2017).
[24]L. Kringle, W. A. Thornley, B. D. Kay, and G. A. Kimmel, "Reversible structural transformations in supercooled liquid water from 135 to 245 K," Science **369**(6510), 1490–1492 (2020).
[25]H. Li, A. Karina, M. Ladd-Parada, A. Späh, F. Perakis, C. Benmore, and K. Amann-Winkel, "Long-range structures of amorphous solid water," J. Phys. Chem. B **125**(48), 13320–13328 (2021).
[26]R. S. Smith, W. A. Thornley, G. A. Kimmel, and B. D. Kay, "Supercooled liquid water diffusivity at temperatures near the glass transition temperature," J. Phys. Chem. Lett. **16**(13), 3198–3205 (2025).
[27]J. M. Parkhurst, A. Cavalleri, M. Dumoux, M. Basham, D. Clare, C. A. Siebert, G. Evans, J. H. Naismith, A. Kirkland, and J. W. Essex, "Computational models of amorphous ice for accurate simulation of cryo-EM images of biological samples," Ultramicroscopy **256**, 113882 (2024).
[28]P. Jenniskens, D. F. Blake, M. A. Wilson, and A. Pohorille, "High-density amorphous ice, the frost on interstellar grains," Astrophys. J. **455**, 389 (1995).
[29]K. P. Stevenson, G. A. Kimmel, Z. Dohnálek, R. S. Smith, and B. D. Kay, "Controlling the morphology of amorphous solid water," Science **283**(5407), 1505–1507 (1999).
[30]U. Raut, M. Famá, B. D. Teolis, and R. A. Baragiola, "Characterization of porosity in vapor-deposited amorphous solid water from methane adsorption," J. Chem. Phys. **127**(20), 204713 (2007).
[31]U. Raut, B. D. Teolis, M. J. Loeffler, R. A. Vidal, M. Famá, and R. A. Baragiola, "Compaction of microporous amorphous solid water by ion irradiation," J. Chem. Phys. **126**(24), 244511 (2007).
[32]J.-H. Fillion, L. Amiaud, E. Congiu, F. Dulieu, A. Momeni, and J.-L. Lemaire, "D_2 desorption kinetics on amorphous solid water: From compact to porous ice films," Phys. Chem. Chem. Phys. **11**(21), 4396–4402 (2009).
[33]D. H. Lee and K. Kim, "Crystallization mechanisms of porous and compact amorphous solid water films," Cryst. Growth Des. **25**(4), 978–985 (2025).
[34]C. Mitterdorfer, M. Bauer, T. G. A. Youngs, D. T. Bowron, C. R. Hill, H. J. Fraser, J. L. Finney, and T. Loerting, "Small-angle neutron scattering study of micropore collapse in amorphous solid water," Phys. Chem. Chem. Phys. **16**(30), 16013–16020 (2014).
[35]E. Mayer and R. Pletzer, "Astrophysical implications of amorphous ice—A microporous solid," Nature **319**, 298–301 (1986).
[36]E. Mayer and R. Pletzer, "Amorphous ice. A microporous solid: Astrophysical implications," Le J. Phys. Colloq. **48**, C1-581–C1-586 (1987).
[37]R. Pletzer and E. Mayer, "Type I isotherms for N_2 adsorption on vapor deposited amorphous solid water," J. Chem. Phys. **90**(9), 5207–5208 (1989).
[38]P. Ehrenfreund, H. J. Fraser, J. Blum, J. H. E. Cartwright, J. M. García-Ruizí, E. Hadamcik, A. C. Levasseur-Regourd, S. Price, F. Prodi, and A. Sarkissian, "Physics and chemistry of icy particles in the universe: Answers from microgravity," Planet. Space Sci. **51**(7–8), 473–494 (2003).
[39]E. F. van Dishoeck, E. Herbst, and D. A. Neufeld, "Interstellar water chemistry: From laboratory to observations," Chem. Rev. **113**(12), 9043–9085 (2013).
[40]C. M. Tonauer, L.-R. Fidler, J. Giebelmann, K. Yamashita, and T. Loerting, "Nucleation and growth of crystalline ices from amorphous ices," J. Chem. Phys. **158**(14), 141001 (2023).
[41]C. S. Boxe, B. R. Bodsgard, W. Smythe, and M. T. Leu, "Grain sizes, surface areas, and porosities of vapor-deposited H_2O ices used to simulate planetary icy surfaces," J. Colloid Interface Sci. **309**(2), 412–418 (2007).
[42]Y. C. Wu, A. Kallis, J. Jiang, and P. G. Coleman, "Structural and phase changes in amorphous solid water films revealed by Positron Beam spectroscopy," Phys. Rev. Lett. **105**(6), 066103 (2010).
[43]C. M. Tonauer, E.-M. Köck, R. Henn, J. N. Stern, L. del Rosso, M. Celli, C. Kappacher, S. Leiter, C. G. Kirchler, C. W. Huck, and T. Loerting, "Near-infrared spectroscopy for remote sensing of porosity, density, and cubicity of crystalline and amorphous H_2O ices in astrophysical environments," Astrophys. J. **970**(1), 82 (2024).
[44]A. Hallbrucker, E. Mayer, and G. P. Johari, "Glass-liquid transition and the enthalpy of devitrification of annealed vapor-deposited amorphous solid water: A comparison with hyperquenched glassy water," J. Phys. Chem. **93**(12), 4986–4990 (1989).
[45]E. Mayer, A. Hallbrucker, G. Sartor, and G. P. Johari, "Glass.fwdarw. Liquid transition and devitrification of $LiCl \cdot 11H_2O$ solution and of hyperquenched and vapor-deposited water," J. Phys. Chem. **99**(14), 5161–5165 (1995).
[46]G. P. Johari, A. Hallbrucker, and E. Mayer, "The dielectric behavior of vapor-deposited amorphous solid water and of its crystalline forms," J. Chem. Phys. **95**(4), 2955–2964 (1991).
[47]C. Gainaru, A. L. Agapov, V. Fuentes-Landete, K. Amann-Winkel, H. Nelson, K. W. Köster, A. I. Kolesnikov, V. N. Novikov, R. Richert, R. Böhmer, T. Loerting, and A. P. Sokolov, "Anomalously large isotope effect in the glass transition of water," Proc. Natl. Acad. Sci. U. S. A. **111**(49), 17402–17407 (2014).

[48]A. L. Agapov, A. I. Kolesnikov, V. N. Novikov, R. Richert, and A. P. Sokolov, "Quantum effects in the dynamics of deeply supercooled water," Phys. Rev. E **91**(2), 022312 (2015).
[49]R. S. Smith and B. D. Kay, "The existence of supercooled liquid water at 150 K," Nature **398**, 788–791 (1999).
[50]Y. P. Handa and D. D. Klug, "Heat capacity and glass transition behavior of amorphous ice," J. Phys. Chem. **92**(12), 3323–3325 (1988).
[51]K. Amann-Winkel, C. Gainaru, P. H. Handle, M. Seidl, H. Nelson, R. Böhmer, and T. Loerting, "Water's second glass transition," Proc. Natl. Acad. Sci. U. S. A. **110**(44), 17720–17725 (2013).
[52]D. Bhattacharya, C. N. Payne, and V. Sadtchenko, "Bulk and interfacial glass transitions of water," J. Phys. Chem. A **115**(23), 5965–5972 (2011).
[53]A. Sepúlveda, E. Leon-Gutierrez, M. Gonzalez-Silveira, C. Rodríguez-Tinoco, M. T. Clavaguera-Mora, and J. Rodríguez-Viejo, "Glass transition in ultrathin films of amorphous solid water," J. Chem. Phys. **137**(24), 244506 (2012).
[54]R. S. Smith, Z. Dohnálek, G. A. Kimmel, G. Teeter, P. Ayotte, J. L. Daschbach, and B. D. Kay, "Molecular beam studies of nanoscale films of amorphous solid water," in *Water in Confining Geometries*, edited by V. Buch and J. P. Devlin (Springer, Berlin, Heidelberg, 2003), pp. 337–357.
[55]F. Perakis, K. Amann-Winkel, F. Lehmkühler, M. Sprung, D. Mariedahl, J. A. Sellberg, H. Pathak, A. Späh, F. Cavalca, D. Schlesinger, A. Ricci, A. Jain, B. Massani, F. Aubree, C. J. Benmore, T. Loerting, G. Grübel, L. G. M. Pettersson, and A. Nilsson, "Diffusive dynamics during the high-to-low density transition in amorphous ice," Proc. Natl. Acad. Sci. U. S. A. **114**(31), 8193–8198 (2017).
[56]M. Ladd-Parada, H. Li, A. Karina, K. H. Kim, F. Perakis, M. Reiser, F. Dallari, N. Striker, M. Sprung, F. Westermeier, G. Grübel, A. Nilsson, F. Lehmkühler, and K. Amann-Winkel, "Using coherent X-rays to follow dynamics in amorphous ices," Environ. Sci.: Atmos. **2**(6), 1314–1323 (2022).
[57]G. Grübel and F. Zontone, "Correlation spectroscopy with coherent X-rays," J. Alloys Compd. **362**(1), 3–11 (2004).
[58]A. R. Sandy, Q. Zhang, and L. B. Lurio, "Hard X-ray photon correlation spectroscopy methods for materials studies," Annu. Rev. Mater. Res. **48**, 167–190 (2018).
[59]A. Madsen, A. Fluerasu, and B. Ruta, "Structural dynamics of materials probed by X-ray photon correlation spectroscopy," in *Synchrotron Light Sources Free-Electron Lasers* (Springer, Cham, 2020), pp. 1989–2018.
[60]F. Lehmkühler, W. Roseker, and G. Grübel, "From femtoseconds to hours—Measuring dynamics over 18 orders of magnitude with coherent X-rays," Appl. Sci. **11**(13), 6179 (2021).
[61]B. J. Berne and R. Pecora, *Dynamic Light Scattering: With Applications to Chemistry, Biology, and Physics* (Dover Publications, 2000).
[62]A. Karina, H. Li, T. Eklund, M. Ladd-Parada, B. Massani, M. Filianina, N. Kondedan, A. Rydh, K. Holl, R. Trevorah, S. Huotari, R. P. C. Bauer, C. Goy, N. N. Striker, F. Dallari, F. Westermeier, M. Sprung, F. Lehmkühler, and K. Amann-Winkel, "Multicomponent dynamics in amorphous ice studied using X-ray photon correlation spectroscopy at elevated pressure and cryogenic temperatures," Commun. Chem. **8**(1), 82 (2025).
[63]S. W. Provencher and P. Štěpánek, "Global analysis of dynamic light scattering autocorrelation functions," Part. Part. Syst. Charact. **13**(5), 291–294 (1996).
[64]R. N. Andrews, S. Narayanan, F. Zhang, I. Kuzmenko, and J. Ilavsky, "Inverse transformation: Unleashing spatially heterogeneous dynamics with an alternative approach to XPCS data analysis," J. Appl. Crystallogr. **51**(1), 35–46 (2018).
[65]T. Eklund, C. M. Tonauer, F. Lehmkühler, and K. Amann-Winkel, "Global q-dependent inverse transforms of intensity autocorrelation data," Photon Sci. (published online 2025).
[66]S. W. Provencher, "A constrained regularization method for inverting data represented by linear algebraic or integral equations," Comput. Phys. Commun. **27**(3), 213–227 (1982).
[67]R. N. Andrews, S. Narayanan, F. Zhang, I. Kuzmenko, and J. Ilavsky, "CONTIN XPCS: Software for inverse transform analysis of X-ray photon correlation spectroscopy dynamics," J. Appl. Crystallogr. **51**(1), 205–209 (2018).
[68]H. Li, M. Ladd-Parada, A. Karina, F. Dallari, M. Reiser, F. Perakis, N. N. Striker, M. Sprung, F. Westermeier, G. Grübel, W. Steffen, F. Lehmkühler, and K. Amann-Winkel, "Intrinsic dynamics of amorphous ice revealed by a heterodyne signal in X-ray photon correlation spectroscopy experiments," J. Phys. Chem. Lett. **14**(49), 10999–11007 (2023).
[69]F. Dallari, A. Martinelli, F. Caporaletti, M. Sprung, G. Grübel, and G. Monaco, "Microscopic pathways for stress relaxation in repulsive colloidal glasses," Sci. Adv. **6**(12), eaaz2982 (2020).
[70]G. A. Kimmel, M. K. Dunlap, K. Gurdumov, R. S. Smith, L. Kringle, and B. D. Kay, "Translational diffusion in supercooled water at and near the glass transition temperature-136 K," J. Chem. Phys. **162**(24), 244505 (2025).
[71]Y. Xu, N. G. Petrik, R. S. Smith, B. D. Kay, and G. A. Kimmel, "Growth rate of crystalline ice and the diffusivity of supercooled water from 126 to 262 K," Proc. Natl. Acad. Sci. U. S. A. **113**(52), 14921–14925 (2016).